Physical properties and pressure-induced superconductivity in the single-crystalline band insulator SnO

Shuxiang Xu,[1,2] Yuting Zou,[1,2] Jianping Sun,[1,2] Ziyi Liu,[1,5] Xiaohu Yu,[1,2,4] Jun Gouchi,[3] Yoshiya Uwatoko,[3] Zhi Gang Cheng,[1,2,4,*] Bosen Wang,[1,2,4,†] and Jinguang Cheng[1,2,4,‡]

[1]*Beijing National Laboratory for Condensed Matter Physics and Institute of Physics, Chinese Academy of Sciences, Beijing 100190, China*
[2]*School of Physical Sciences, University of Chinese Academy of Sciences, Beijing 100190, China*
[3]*Institute for Solid State Physics, University of Tokyo, Kashiwanoha 5-1-5, Kashiwa, Chiba 277-8581, Japan*
[4]*Songshan Lake Materials Laboratory, Dongguan, Guangdong 523808, China*
[5]*School of Physics, Harbin Institute of Technology, Harbin 150001, China*

(Received 9 July 2019; revised manuscript received 19 January 2020; accepted 29 January 2020; published 2 March 2020)

We report the growth and physical properties of high-quality single-crystal SnO via electrical transport, specific heat, Hall coefficients, and the high-pressure effect. Apart from polycrystalline SnO showing an insulating behavior in the whole temperature range, the in-plane resistivity ρ_{ab} of single-crystal SnO exhibits a metal-insulator transition around the characteristic temperature T_{M-I}. The anisotropic resistivity ratio ρ_c/ρ_{ab} is $\sim$1 for $T \geqslant T_{M-I}$ and increases quickly up to $\sim$400 for $T < T_{M-I}$, which implies the enhanced anisotropic electronic structures and electronic correlations. Its multiband electronic character with dominant hole-type carriers is revealed via the Hall coefficient and the appearance of low-lying phonon models, evidenced by specific heat showing an evident peak at $\sim$10 K in $(C_p - \gamma_n T)/T^3$ vs T. The appearance of a metal-insulator phase transition in single-crystal SnO was attributed to the slight difference in the lattice parameters ratio c/a, the atomic coordinate of Z(Sn), and the chemical pressure effect. Under hydrostatic pressures generated in a cubic-anvil pressure cell, the insulating state melts at the critical pressure $P_c \sim 3-4$ GPa, and the temperature exponent of resistivity $\rho \propto T^n$ in the metallic state increases gradually from $n = 2$ to 3 with increasing the pressure. A domelike superconductivity is achieved in the diamond pressure cell with the pressure up to 13.5 GPa and the temperature to 80 mK, with the superconducting transition temperatures and the upper critical fields close to those of polycrystals. Several possible physical mechanisms are proposed.

DOI: 10.1103/PhysRevB.101.104501

I. INTRODUCTION

Iron-based superconductors (SCs) are widely thought to arise from bad metal and/or semimetal by chemical doping and pressure [1–3], different from the antiferromagnetic insulator and/or charge ordered states in copper-based high-T_c SCs [4–6]. It is of great significance to build a bridge between them to understand the underlying superconducting mechanisms [4,5]. In this regard, insulating and analog materials to iron-based SCs are interesting and might serve as a bridge to connect these two classes of high-T_c SCs [3,7]. This can advance both theories and experiments [5]. Generally, the melting of an insulating state via external parameters involves interesting issues, e.g., the metal-insulator transition [8], and superconductivity [1,2]. The latter is interesting, with anisotropic bands and electronic correlations for layered crystals.

In this regard, tetragonal-phase SnO is an ideal example [9]. It crystallizes in the α-PbO structure (space group, SG: $P4/nmm$) with the stacked SnO layers connected by weak van der Waals interactions [9–11]. In comparison with isostructural FeSe, the metallic and nonmetallic elements are interchanged, i.e., the oxygen (tin) in SnO corresponds to iron (selenium) in FeSe [3]. Strong charge repulsion between the Sn^{2+} cations prevents the insertion of other cations (e.g., K^+ and Ca^{2+}) into the SnO layers [12]. Meanwhile, distinct electrical transport and magnetic properties have been reported accordingly [2,3,13]. FeSe is metallic and undergoes a structural/nematic phase transition at $T_s \approx 90$ K prior to the superconducting state below 8 K [14], while SnO is an indirect-gap semiconductor/insulator with an energy gap $E_g \sim 0.7$ eV [11,15]. Interestingly, SnO shows unusual superconductivity along with the metallization under pressure at 5–6 GPa [13]. Similar superconducting phase diagrams in SnO to the Fe-based SCs have attracted attention, but the underlying mechanism remains elusive until now. Infrared spectroscopy has been preformed to confirm the energy gap closure under pressure [11,15]. Based on the results of the theoretical calculations [13,16–18], SnO was argued to have a similar Fermi surface topology as those of Fe-based SCs [1,2,13] and that the nesting of hole and electron pockets closely correlates with the superconductivity and the change of T_c as a function of pressure [17]. Naturally, a comparative study compared with various known unconventional SCs is

*zgcheng@iphy.ac.cn
†bswang@iphy.ac.cn
‡jgcheng@iphy.ac.cn

required, and these similarities stimulate studies on superconductivity and mechanisms of this system [13].

For SnO, several issues are still controversial, as reported in [14,16]. The first one is whether the superconductivity correlates with structural abnormality or not, e.g., is there a structural transition and phonon anomaly [11,19]. It was found that whether the second-order tetragonal-orthorhombic structural transition appears under pressure strongly depends on pressure conditions [19–21]. According to the reports by Adams and Zhang, SnO shows a tetragonal-orthorhombic structural transition [19]. But there is no structural transition if using a uniaxial pressure apparatus with solid pressure mediums [20,21]. Meanwhile, theoretical analyses considering the electron-phonon interactions have revealed the importance of the out-of-plane motions of O atoms along the c axis and the Sn-s lone pairs for superconducting pairing [18]. This means that the phonon anomaly associated with lattice instabilities can be an important factor affecting superconductivity as for other conventional SCs. For all the previous studies based on polycrystal SnO, grain boundaries, disorder, and strain are unavoidable [22,23], and thus it is essential to carry out comprehensive studies on high-quality single-crystal samples under hydrostatic pressure conditions, which are still lacking for single-crystal SnO.

In this work, we report the growth and detailed characterizations of high-quality single-crystal SnO grown by hydrothermal methods and physical properties of single-crystal SnO. It is found that the in-plane resistivity ρ_{ab} shows a metal-insulator transition on cooling at T_{M-I}, and the anisotropic ratio ρ_c/ρ_{ab} is $\sim$1 for $T \geqslant T_{M-I}$ but increases up to $\sim$400 for $T < T_{M-I}$. With increasing the pressure, the ground state melts into a metallic phase at $P_c \sim 3-4$ GPa and the evolution of the correlative parameters is summarized. The "domelike" superconductivity is observed in a diamond pressure cell up to 13.5 GPa and down to 80 mK.

II. EXPERIMENTAL METHODS

A. Single crystal

Single-crystal SnO was grown by adopting a modified hydrothermal method with $SnCl_2 \cdot 2H_2O$ (99.99%) and NaOH (99.99%) [12]. First, 40 mL NaOH aqueous solution, $\sim$0.40 mol/L and 20 mL of $SnCl_2 \cdot 2H_2O$ aqueous $\sim$0.20 mol/L, were mixed and stirred for 30 min with a magnetic stirrer at a rate of 1000 r/min. The yellow turbid liquid was transferred to an autoclave ($\sim$100 mL) and then heated at 100 °C and 170 °C for 28 h. The products were washed in deionized water. The obtained crystals were dried at 60 °C for 8 h in a drying oven.

B. Characteristic of structures/compositions

Single-crystal x-ray diffraction (XRD) was performed using a DX2700B diffractometer. Powder XRD was accomplished using a Huber G670-V42833-3 diffractometer (Cu $K\alpha$, $\lambda = 1.5406$ Å). Refinements were performed using FULLPROF software to extract the structural parameters [24]. The Sn/O ratio was indicated (1:1.02) by energy dispersive x-ray analysis (EDX). Thermogravimetric analysis was carried out in an atmosphere of H_2(5%)/Ar(95%) and Ar to estimate the real oxygen concentration. X-ray photoelectron spectrum (XPS) analysis was also preformed to confirm the Sn valence state in single-crystal SnO.

C. Physical properties at ambient pressure

Electrical transport, the Hall coefficient, and heat capacity were measured on a Quantum Design physical property measurement system (PPMS-9T). The four-probe method was used for resistivity measurements. An antisymmetrized method was adopted to obtain transverse resistivity and the Hall coefficient.

D. Hydrostatic pressure effect

A palm-type cubic-anvil cell (CAC) apparatus was employed [25]. CAC can generate hydrostatic pressure with the multiple-anvil geometry. The MgO cubes were used as gasket and the glycerol as a pressure transmitting medium (PTM). All the measurements were performed in a ^{4}He refrigerated chamber ($1.4\ K \leqslant T \leqslant 295$ K).

E. High-pressure effect in a diamond pressure cell

Resistivity $\rho(T)$ was measured in a Be-Cu-type diamond anvil cell (DAC) with 500-μm flats for high-pressure stability. The four-probe method was adopted with soft KBr powder as the PTM, which is widely used for high-pressure studies. All the measurements were carried out in a dilution refrigerator ($10\ \text{mK} \leqslant T \leqslant 295$ K).

III. RESULTS AND DISCUSSION

Figures 1(a) and 1(b) show the crystal structure of the tetragonal phase of SnO, which is featured by the SnO layers stacked along the c axis. For each layer, the oxygen atoms are surrounded tetrahedrally by four tin atoms, and a tin atom is bonded to four oxygen atoms, forming a regular square pyramid [12,16]. This structure can be also viewed by exchanging Fe and Se atoms in β-FeSe [2,3]. This analogy is closely related to similar bands with both electron and hole pockets [13]. We note that the morphology and the geometry of as-obtained SnO differ with the reaction temperature T_s ($\sim$100 °C, 170 °C, and 185 °C). As shown in the inset of Fig. 1(c), single-crystal SnO is starlike for $T_s \sim 100$ °C and is platelike in shape for $T_s \sim 170$ °C, which indicates different oxygen concentration as evidenced by room-temperature XRD. In Fig. 1(c), XRD of single-crystal SnO with $T_s \sim 170$ °C was taken as an example. (00l), (002), and (004) diffraction peaks exist, indicating that the natural dissociation surfaces and the preferred growth orientation of the single crystals are parallel to the ab plane. Powder XRD was measured on pulverizing single crystals and refined using a tetragonal α-PbO structure (SG: $P4/nmm$, No. 129) [12] in Figs. 1(d) and 2(a)–2(c). The refined structural parameters are listed in Table I and single-crystal XRD results in the Supplemental Material [26]. It is found that both lattice parameters and volume expand with increasing the reaction temperature T_s. An explanation for such a trend is that real oxygen concentration increases with T_s. However, for $T_s \sim 185$ °C, close to the phase boundary of SnO-SnO_2, yellow particles (SnO_2) are embedded and cannot be separated easily [27]. In

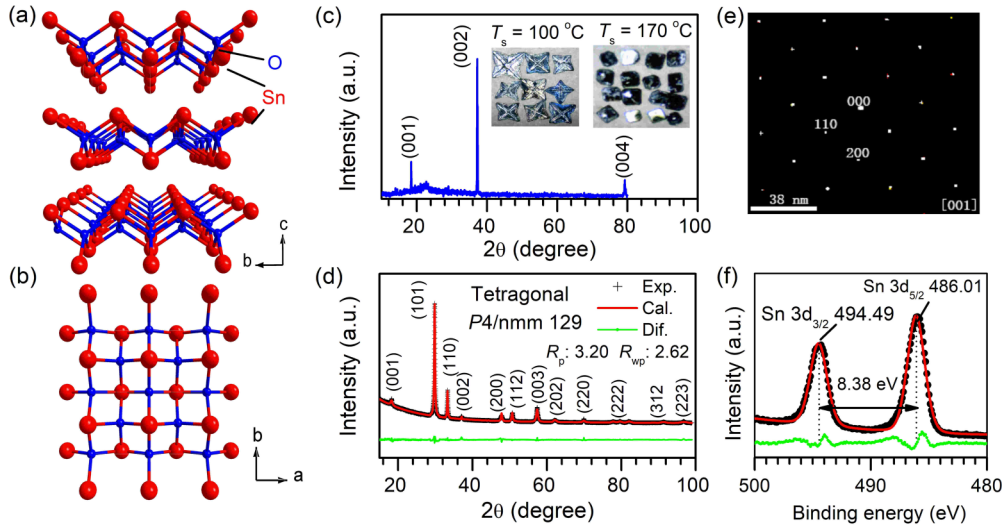

FIG. 1. Crystal structures of tetragonal SnO projected to (a) (100) and (b) (001), respectively. (c) Single-crystal x-ray diffraction (XRD) pattern of SnO for $T_s = 170$ °C. Inset shows the morphological characteristics of crystals. (d) The refinement of powder XRD for $T_s = 170$ °C. (e) Laue diffraction of single-crystal. (f) X-ray photoelectron spectroscopy (XPS) of Sn-3d signals. The experimental data is shown by black solid circle and the fitting by the red line.

Figs. 2(d)–2(f), we note that the lattice parameters are close to the stoichiometric SnO determined by x-ray diffraction and neutron diffraction [11,19], but all the parameters of the previously reported single crystals are slightly larger [12]. Thus we focused on the crystals with $T_s \sim 100$ °C and 170 °C.

Figure 1(e) shows the Laue diffraction pattern of single-crystal SnO along the [00l] directions, which confirms the well-defined tetragonal phase of single-crystal SnO. The XPS analysis is conducted to confirm the composition of Sn and O, as well as the valence state of Sn. It is found that the Sn-3d spectrum split into $3d_{5/2}(J = 5/2)$ and $3d_{3/2}(J = 3/2)$ components with the spin-orbit splitting energy ~8.38 eV in Fig. 1(f). The binding energies at ~494.49 and ~486.01 eV correspond to spectral bands of Sn-$3d_{3/2}$ and Sn-$3d_{5/2}$, respectively, or Sn^{2+} [12,21]. Thermogravimetric analysis was also performed in the atmosphere of H_2(5%)/Ar(95%) and pure Ar in Figs. 3(a)–3(d). Clear weight loss exists in the atmosphere of H_2(5%)/Ar(95%), and the calculated Sn:O ratio is ~1:1.02. Meanwhile, EDX was preformed to further confirm the Sn/O ratio of ~1:1.02 in Figs. 3(e) and 3(f) (see Table II), and the absence of chlorine (the K_a of Cl, ~2.621 eV).

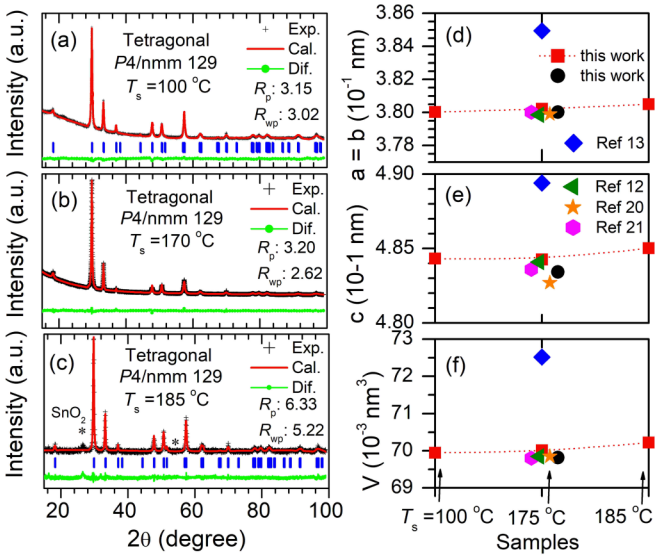

FIG. 2. Refinement of powder XRD for (a) $T_s = 100$ °C, (b) $T_s = 170$ °C, and (c) $T_s = 185$ °C, respectively. The comparison of lattice parameters: (d) lattice parameter $a = b$; (e) lattice parameter c; (f) volume.

Figure 4 displays the temperature dependence of $\rho(T)$ for single-crystal and polycrystalline SnO. For the former, the in-plane resistivity ρ_{ab} is comparable and changing with different T_s. For each single crystal, ρ_{ab} exhibits a metal-insulator transition at T_{M-I}, which is defined as the minimum of $\rho(T)$ as marked in Figs. 4(a)–4(c). In contrast, $\rho(T)$ of polycrystalline SnO shows an insulating behavior below 300 K as reported. The value of T_{M-I} increases with increasing T_s and shows a positive correlation with the lattice parameters. The band gap E_g is obtained by a linear fitting to $\ln \rho(T)$ vs $1/T$ according to the thermal-activation model in Figs. 4(e)–4(g) [8]. As shown in Figs. 4(i) and 4(j), E_g exhibits an increasing trend with increasing the value of T_s, similar to that of T_{M-I}. As shown in Fig. 4(d), with decreasing the pressure, the out-of-plane resistivity ρ_c shows a weak temperature dependence at first and then a pronounced enhancement, with no clear evidence of a metal-insulator transition. The anisotropic resistivity ratio ρ_c/ρ_{ab} is ~1 for $T \geqslant T_{M-I}$ and increases up to ~400 below T_{M-I}, evidencing a strong anisotropic electronic structure and electronic correlations [13,16,18]. At ambient pressure (AP), the value of E_g from ρ_c is ~27.3 meV and comparable to that of a polycrystal (~28.5 meV). And both values are smaller than ~0.70 eV, obtained by measuring the infrared spectroscopy [11,15]. But in Fig. 4(i), E_g is only ~3−15 meV as obtained from the ρ_{ab} data, which is one order smaller in magnitude than that from ρ_c. Thus, these characterizations demonstrate that SnO has an anisotropic electronic structure [16,18].

TABLE I. Crystallographic parameters for SnO with different T_s.

T_s (°C)	100	170	185
Crystal system	Tetragonal	Tetragonal	Tetragonal
Space group	$P4/nmm$ 129	$P4/nmm$ 129	$P4/nmm$ 129
a, b (Å)	3.80028(2)	3.80221(5)	3.80503(6)
c (Å)	4.84324(7)	4.84262 (6)	4.85021(5)
V (Å^3)	69.9466(6)	70.0081(3)	70.2213(8)
c/a or c/b	1.2744(5)	1.2736(8)	1.2747(3)
Sn $(x/y/z)$	0.75/0.75/0.2726(3)	0.75/0.75/0.2758 (6)	0.75/0.75/0.2736(3)
O $(x/y/z)$	0.25/0.75/0.50	0.25/0.75/0.50	0.25/0.75/0.50
R_P (%)	3.154	3.203	6.325
R_{WP} (%)	3.021	2.620	5.223
χ^2	5.382	5.889	8.335

Figures 5(a) and 5(b) show the Hall resistivity $\rho_{xy}(H)$ for $T_s = 100$ °C and 170 °C. $\rho_{xy}(H)$ shows a linear field dependence, and its positive slope decreases with increasing temperature, which suggests that hole-type carriers dominate in SnO. The Hall coefficient $R_H = d\rho_{xy}/dH$ is obtained from the linear fittings and its temperature dependence as plotted in Figs. 5(c) and 5(d). It is found that the magnitude of $|R_H|$ decreases slightly and tends to level off above 200 K. Such behaviors occur in many multiband materials [28]. To simplify the analysis, the hole-type carrier concentration is estimated as $n = 1/|R_H e|$ by assuming a single-band model. As shown in Fig. 5(e), n is $\sim 6.05 \times 10^{19}$ cm^{-3} at $T < 50$ K and increases to $\sim 14.19 \times 10^{19}$ cm^{-3} at 200 K. A similar enhancement of n is found for $T_s = 170$ °C but with a slightly higher value in Fig. 5(f), which is consistent with the evolution of T_{M-I}, E_g with T_s as mentioned above.

Figure 6(a) shows $C_p(T)$ of SnO, which increases with increasing temperature and reaches the saturated value $\sim 3NR = 49.9$ J/mol K at 300 K. The inset shows the low-T $C_p(T)$ as $C_p(T)/T$ vs T^2, which is linearly fitted by the formula $C_p/T = \gamma_n + \beta_n T^2$ for the data of $2 \leqslant T \leqslant 5$ K, where the γT and βT^3 terms represent electronic and phonon contributions, respectively. It gives a Sommerfeld coefficient of $\gamma_n = 0.176$ mJ/mol K^2, and $\beta_n = 0.309$ mJ/mol K^4. The value of γ_n is close to zero, and the Debye temperature $\Theta_D = 184.6$ K is calculated by $\beta_n = 12\pi^4 NR/5\,\Theta_D^3$ (where $N = 2$, and R is the gas constant). To extract the information of the phonon, $(C_p - \gamma T)/T^3$ is plotted in Fig. 6(b). It shows a broad peak at ~10 K, manifesting the existence of low-energy Einstein vibration modes in the phonon spectrum [29,30], which usually occurs in unstable materials with enhanced electron-phonon coupling and superconductivity [31].

Figure 7 shows the $\rho_{ab}(T)$ under various hydrostatic pressures in CAC up to 12.5 GPa. For $T_s = 100$ °C, the value of $T_{M-I} \sim 123$ K at AP decreases gradually to ~89 K with increasing the pressure up to 2 GPa. Upon increasing the pressure further, the metal-insulator transition shifts progressively to lower temperature and a metallic state appears for

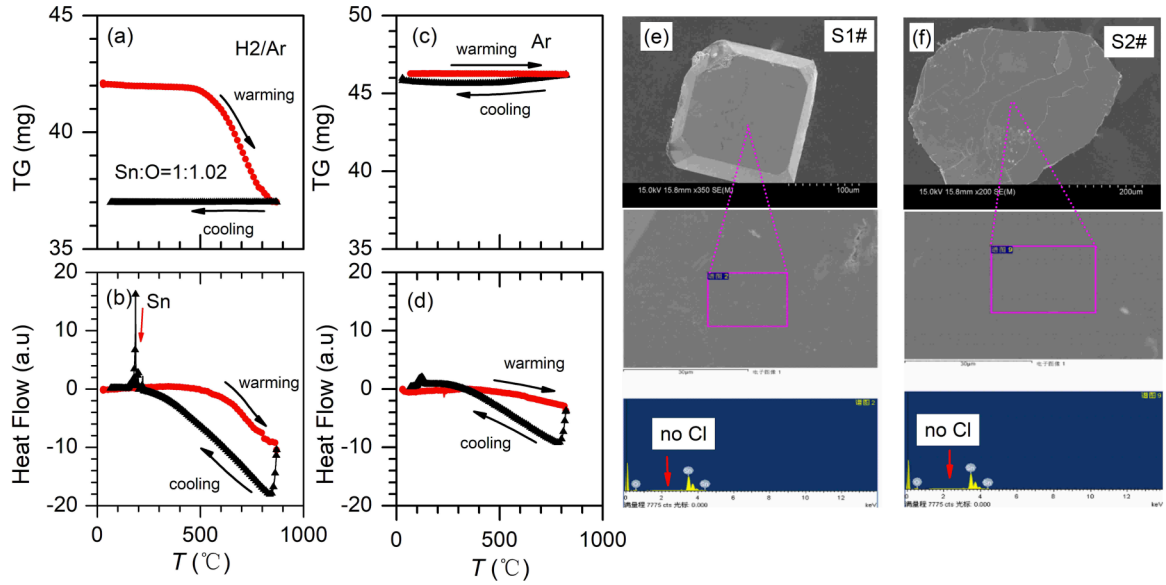

FIG. 3. Thermogravimetric analysis in the atmosphere of (a, b) H_2(5%)/Ar(95%) and (c, d) pure Ar. The ratio of Sn/O is estimated to 1:1.02. The arrows indicate warming/cooling processes, and the peak in Fig. 3(b) shows a solid-liquid phase transition of Sn. (e, f) Energy dispersive x-ray analysis (EDX) and the ratio of Sn/O is close to 1:1, and there is no chlorine ($K\alpha$ of Cl element, ~2.621 eV).

TABLE II. EDX results of Sn/O ratio for various samples.

Sample nos.	SnO/Sn/O ratio
S1#_part1	1:1:0.977
S1#_part2	1:1:1.099
S2#_part1	1:1:1.181
S2#_part2	1:1:1.189
S3#	1:1:1.023
S4#_part1	1:1:1.165
S4#_part2	1:1:1.230
S5#	1:1:1.182
S6#	1:1:1.044
S7#_part1	1:1:0.927
S7#_part2	1:1:1.065
Average ratio of Sn/O	1:1:1.02

$P > 4$ GPa, which suggests that the indirect band gap is closed completely by pressure. Similarly, for $T_s = 170$ °C, $T_{M-I} \sim 130$ K at AP is undetectable for $P > 3$ GPa. We note that the critical pressures are smaller than the values obtained from high-pressure studies of infrared spectroscopy (5–6 GPa) [15], which originates from the anisotropic energy gaps of single crystals. With increasing the pressure further, ρ_{ab} decreases monotonously. ρ_{ab} at 12.5 GPa is about three orders of magnitude smaller than that at AP. Moreover, for $T_s = 100$ °C, an abnormal upturn appears at around $T^* \sim 5.5$ K at $P > 5$ GPa. With increasing the pressure, the amplitude of the upturn decreases while T^* is invariant with increasing the pressure and the external magnetic field, which eliminates the interference of magnetic impurities. This upturn of ρ_{ab} is strange and disappears for $T_s = 175$ °C, and some extrinsic factors may be responsible. At low temperature, there is no sign of superconductivity down to 1.4 K for 9.0, 9.5 GPa, which is much closer to the maximum T_c of the superconducting phase diagram [13]. We note that the resistivity of single-crystal SnO at 2 K is ~35 $\mu\Omega$ cm at 12.5 GPa for $T_s = 100$ °C and ~5 $\mu\Omega$ cm at 9.0 GPa for $T_s = 175$ °C, which are smaller than those of polycrystalline SnO at similar pressure (~100 $\mu\Omega$ cm at 15 GPa). In comparison with previous reports [13], the polycrystalline sample and uniaxial pressure may be the critical difference.

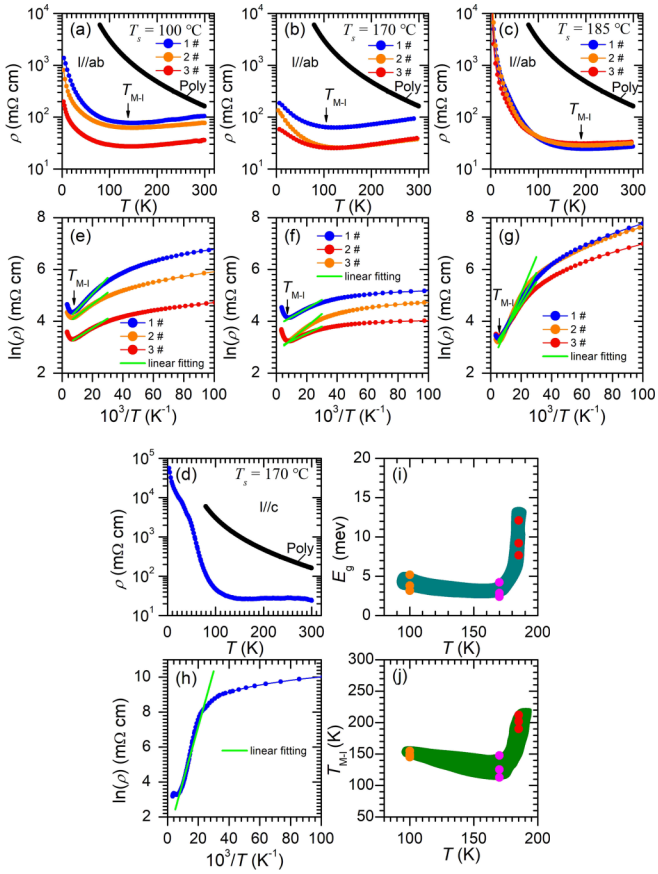

FIG. 4. $\rho_{ab}(T)$ for (a) $T_s = 100$ °C; (b) $T_s = 170$ °C; (c) $T_s = 185$ °C; (d) $\rho_c(T)$ for $T_s = 170$ °C; (e)–(h) log-scale $\rho_{ab}(T)$. The green lines are the linear fittings. T_{M-I} is marked by black arrows. The energy gaps obtained from the linear fittings (e)–(h) and T_{M-I} (a)–(d) vs T_s are plotted in Figs. 4(i)–(j).

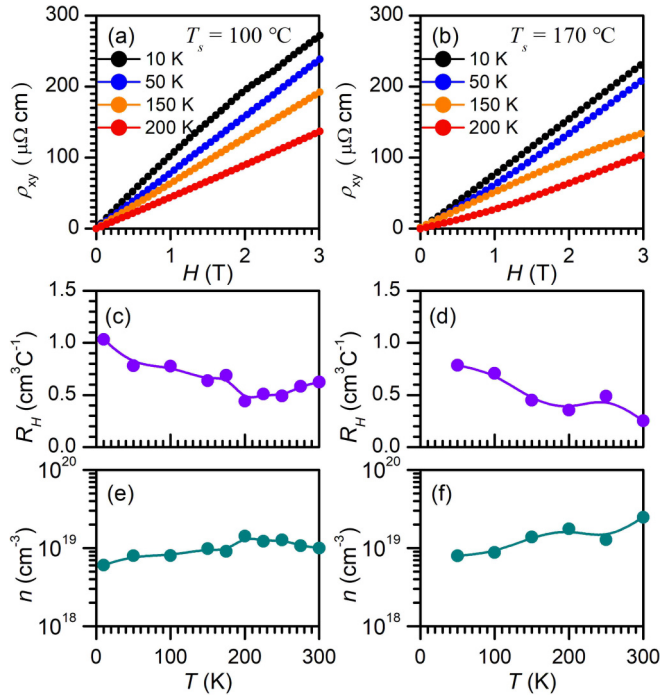

FIG. 5. $\rho_{xy}(H)$ for (a) $T_s = 100$ °C and (b) $T_s = 170$ °C. R_H and carrier density n extracted from $\rho_{xy}(H)$, $R_H = d\rho_{xy}/dH$, and $n = 1/(R_H e)$ at each temperature for $T_s = 100$ °C (a, c, e) and $T_s = 170$ °C (b, d, f), respectively.

To search for SC at lower temperature, we performed high-pressure resistivity on single-crystal SnO by using a diamond anvil cell with soft pressure medium KBr down to 80 mK in a dilution refrigerator. As in Fig. 8(a), for the first run ($P = 2$, 9.5, 13.5 GPa), the temperature dependence of ρ_{ab} decreases gradually by 3–4 orders of magnitude with the increase of pressure, which is consistent with the results using a CAC. Further low-temperature tests in Fig. 8(b) ($P = 5.5$, 7.0, 8.5, 10 GPa) show that SnO enters into the superconducting state with a sharp drop in resistivity. Superconducting transition temperatures are marked by T_c^{onset} and T_c^{zero}, respectively, which are defined as the temperatures where resistivity departs from linear behavior

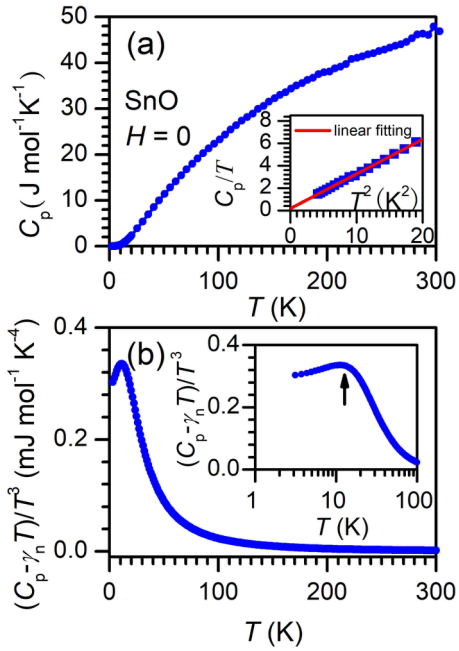

FIG. 6. (a) Heat capacity $C(T)$ vs T. The inset shows $C_p(T)/T$ and its polynomial fittings $C_p/T = \gamma + \beta T^2$ for $2 \leqslant T \leqslant 5$ K, where γT and βT^3 are electron and phonon contributions. (b) $(C_p - \gamma_n T)/T^3$ vs T, and the inset shows the enlargement at low temperature.

and reaches zero, respectively. T_c^{onset} increases up to ~1.55 K at 5.5 GPa, ~1.60 K at 7.0 GPa, and ~1.82 K at 8.5 GPa at first and then decreases with increasing pressure. T_c^{zero} is ~0.89 K at 7.0 GPa and ~0.55 K at 8.5 GPa at first and then decreases with increasing pressure. The pressure

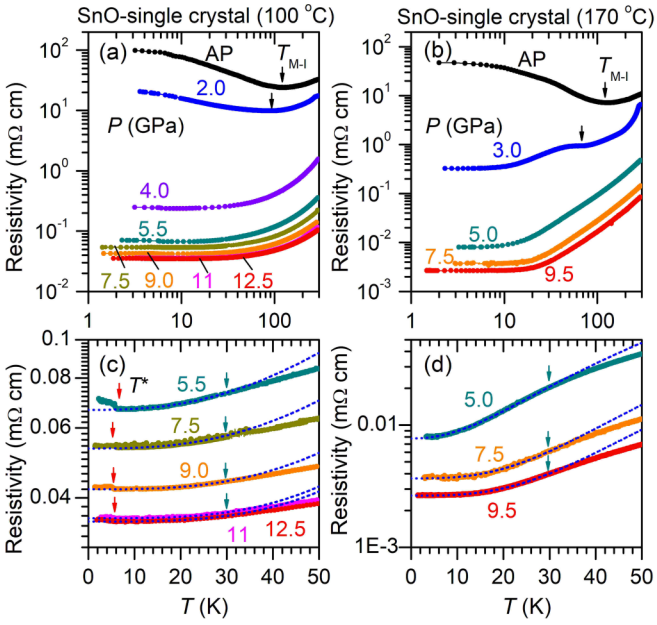

FIG. 7. $\rho_{xy}(T)$ and its enlargement pattern for $T_s = 100$ °C (a, c) and 170 °C (b, d). The blue lines in (c) and (d) represent the fitting curves of $\rho = \rho_0 + AT^n$. The black arrows in (a) and (b) represent the T_{M-I}. The red arrows in (c) represent the abnormal temperature T^*.

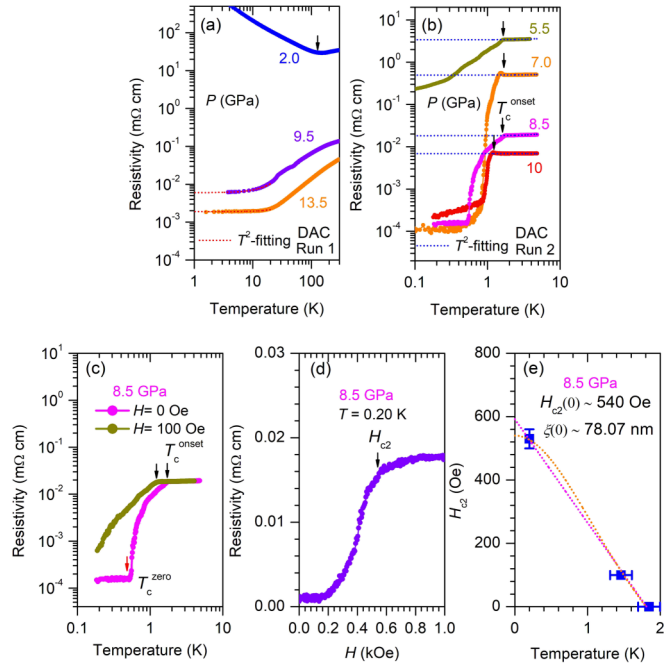

FIG. 8. (a) $\rho_{ab}(T)$ for the first run in DAC with $P = 2$, 9.5, and 13.5GPa. (b) Low-T $\rho_{ab}(T)$ for the second run with $P =$ 5.5, 7.0, 8.5, and 10 GPa. (c) $\rho_{ab}(T)$ at 0, 100 Oe for 8.5 GPa. (d) $\rho_{ab}(H)$ at 0.20 K and 8.5 GPa. (e) The upper critical field $H_{c2}(T)$ and the fittings by the Werthamer-Helfand-Hohenberg formula $H_{c2}(0) = -0.693 T_c dH_{c2}/dT$ and the Ginzburg-Landau equation $H_{C2}(T) = H_{C2}(0)[1 - (T/T_c)^2]/[1 + (T/T_c)^2]$, respectively.

dependence of T_c^{onset} and T_c^{zero} are summarized in Fig. 9. For 8.5 GPa, we also measured field-dependent $\rho(T)$ and $\rho(H)$ at 0.20 K in Figs. 8(c) and 8(d), from which the upper critical field $H_{c2}(0)$ is estimated to be 540 Oe at 8.5 GPa by the Werthamer-Helfand-Hohenberg formula $H_{c2}(0) = -0.693 T_c dH_{c2}/dT$ and the Ginzburg-Landau equation $H_{C2}(T) = H_{C2}(0)[1 - (T/T_c)^2]/[1 + (T/T_c)^2]$, respectively [32]. $H_{C2}(0)$ is ~1.5% of the Pauli paramagnetic limited upper critical field of $1.84 T_c \sim 33.2$ kOe for an isotropic SC. In Bardeen-Copper-Schrieffer (BCS) theory,

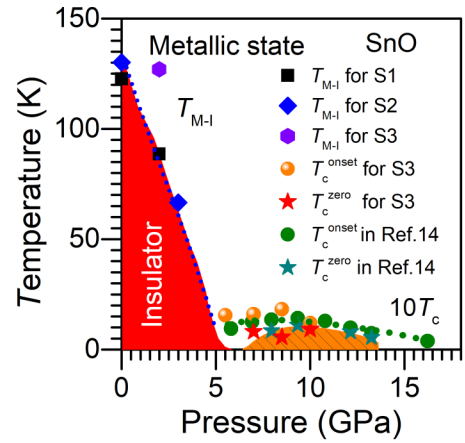

FIG. 9. Phase diagram of SnO. The values of T_{M-I}, T_c^{onset}, and T_c^{zero} are determined from high-pressure resistivity. The thick line indicates the tendency.

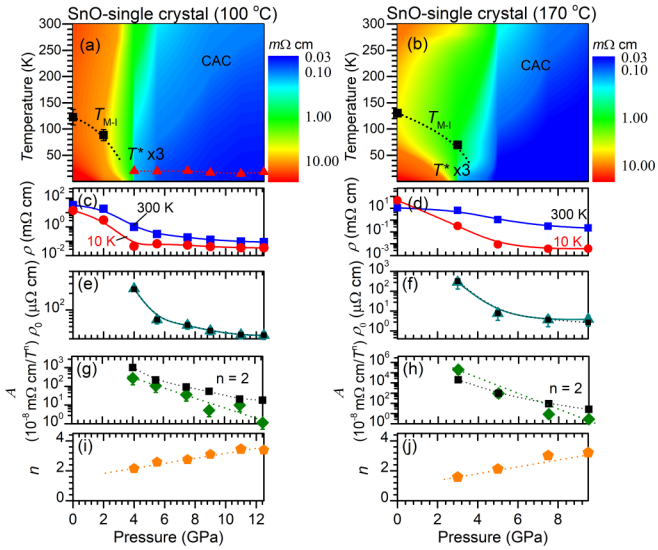

FIG. 10. All the parameters with pressure: (a, b) Temperature-pressure diagram, (c, d) the isothermal resistivity, (e, f) residual resistivity ρ_0 by fitting $\rho = \rho_0 + AT^n$, (g, h) the coefficient A, (i, j) the exponent n for $T_s = 100$ °C and 170 °C.

$H_{C2}(0) = \Phi_0/2\pi\xi(0)^2$ (where $\Phi_0 = hc/2e$ is the magnetic flux quantum and $\xi(0)$ is the coherent length). Thus, $\xi(0) \sim 78.07$ nm. The lower $H_{C2}(0)$ and larger $\xi(0)$ indicate SnO may be close to type-II SC in the weak correlation limitations [31,32]. Further studies of bulk superconductivity need magnetic susceptibility under pressure. It is sure that the uniaxial pressure enhances the superconducting transition temperature compared with CAC, and it is thought that different evolutions of crystal and electronic structure with pressure in the DAC and CAC apparatus are critical.

Low-T $\rho(T)$ was analyzed with the empirical formula $\rho = \rho_0 + AT^n$ in Figs. 7(c), 7(d), 8(a), and 8(b), where ρ_0 represents residual resistivity, and the temperature coefficient $A(P)$ and the exponent $n(P)$ are related to the inelastic electron scattering. The fitting curves are plotted in Figs. 7(c), 7(d), 8(a), and 8(b). The pressure-dependent parameters are summarized and plotted in Fig. 10. The values of T_{M-I} and T^* are also compared, and the color represents the changing trend of resistivity. For both samples, T_{M-I} decreases more rapidly when approaching P_c as the closure of band gaps. Interestingly, for $T_s = 100$ °C, the magnitude of $\rho(T)$ at 12.5 GPa is reduced by ~375 times (300 K) and ~400 times (10 K) compared to that at AP, as in Fig. 10(c). For $T_s = 170$ °C, the magnitude of $\rho(T)$ at 9.5 GPa is reduced by ~3000 times (300 K) and ~100 000 times (10 K) compared to that at AP in Fig. 10(d). The changes in resistivity of the single crystal well reflect those of the intrinsic electronic structure without grain boundaries. In Figs. 10(e)–10(j), several features are found: $\rho_0(P)$ reduces monotonously with increasing pressure, two orders lower in magnitude compared to that at AP, while $n(P)$ increases from ~2.1 at 4 GPa to ~3.1 above 9 GPa for $T_s = 100$ °C, and from ~1.58 at 3 GPa to ~3.2 at 9.5 GPa for $T_s = 170$ °C. In general, the exponent n is correlated with energy bands, disorders, and dimensionality, etc. Disorder is avoided and crystal anisotropy seems not to be sensitive. The results demonstrate that the changes of $n(P)$ are derived from different scattering mechanisms [31,33]. For example, T^2 dependence shows that electron-electron scattering is a main source while T^5 dependence indicates important electron-phonon scattering.

Temperature-pressure phase diagrams are plotted for single-crystal and polycrystalline SnO. As shown in Fig. 10(a), T_{M-I} reduces gradually by pressure and a metallic state appears at ~3–4 GPa for single-crystal SnO and ~5–6 GPa for polycrystalline SnO [13,15,19]. Theoretical calculations have demonstrated that pressure-induced metallization mainly stems from the transformation of weakly hybridized O-2p, Sn-5s, Sn-5p subband, the lowest valence state of Sn-3d states [16,18]. And the electronic states from O-2p and Sn-5s states at the Fermi level increase immediately with increasing pressure, which results in the band-gap closure. The slight difference in the critical pressure of metallization originates from little differences in lattice parameters, theoretical models, and errors in pressure calibrations [18]. The pressure dependence of the quadratic temperature coefficient $A(P)$ (for $n = 2$) is plotted in Figs. 10(g) and 10(h).

Finally, several important issues need to be clarified. The first one is the observation of the metal-insulator phase transition in single-crystal SnO that is absent in polycrystalline SnO. The characteristic of single-crystal SnO can eliminate the possibility of impurities. As we know, SnO is anisotropic along the ab plane and the c direction. We note that the c/a ratio of single-crystal SnO is reduced slightly compared with those of other reports [8,11,16], while the atomic coordinate of Z(Sn) is a little larger accordingly. This means that single-crystal SnO experiences a slight chemical pressure [16,18], and the weakly hybridized O-2p and Sn-5s might account for the appearance of the metal-insulator phase transition and the differences in the critical pressures of metallization. The second issue is whether the superconductivity is correlative with structural transition and phonon anomaly. It is sure that there is no signature of structural transition under pressure, but a phonon anomaly exists. $(C_p - \gamma T)/T^3$ shows a peak at ~10 K, manifesting the existence of anomalous low-energy phonons [29,30], which is important glue for superconducting pairings. Whether this abnormal behavior is related to the change of Z(Sn) is not clear at this moment, but its contribution is important to the emergence of superconductivity without pressure-induced structural transition. It is pointed out via theoretical calculations that the out-of-plane motions of O atoms and Sn-s lone pairs is important [18]. The third one is the possible superconducting mechanism and the origin of a "domelike" superconducting diagram. Based on these analyses, it is thought that SnO under pressure belongs to weakly coupled phonon-mediated SCs under pressure, which comes from the enhanced interactions between hole and electron pockets. Further studies on the phonon spectrum and susceptibility are required to understand the details of superconductivity of this system.

IV. CONCLUSION

In summary, we report anisotropic physical properties of high-quality single-crystal SnO as well as the high-pressure effect. An anisotropic electronic state is revealed with the ratio $\rho_c/\rho_{ab} \sim 400$ at lower temperature. The Hall coefficient suggests its multiband features with dominant hole-type

carriers. The temperature dependence of $(C_p - \gamma_n T)/T^3$ shows a peak at ~10 K, indicating the appearance of low-lying phonon modes. Under hydrostatic pressure, the insulating state melts at the critical pressure $P_c \sim 3-4$ GPa, and the temperature exponent of resistivity in the metallic state increases from $n = 2$ to $n = 3$ with increasing pressure. Meanwhile, a "domelike" superconductivity is achieved with superconducting transition temperature and an upper critical magnetic field close to those of polycrystalline samples.

ACKNOWLEDGMENTS

We are grateful to Prof. H. C. Lei, Prof. Q. H. Zhang, Prof. L. Gu, Prof. B. J. Feng, Prof. F. Hong, Prof. X. Luo, and Prof. M. Q. Xue for useful help and discussions. This work is supported by the National Key Research and Development Program of China (Grants No. 2018YFA0305700 and No. 2018YFA0305800), the National Natural Science Foundation of China (Grants No. 11874403, No. 11574377, No. 11834016, and No. 11874400), the Beijing Natural Science Foundation (Grant No. Z190008), the Strategic Priority Research Program and Key Research Program of Frontier Sciences of the Chinese Academy of Sciences (Grants No. XDB25000000 and No. QYZDB-SSWSLH013), the CAS interdisciplinary Innovation Team, IOP Hundred-Talent Program (Grant No. Y7K5031 × 61), and the Youth Promotion Association of CAS (Grant No. 2018010).

[1] C. de la Cruz, Q. Huang, J. W. Lynn, J. Li, W. Ratcliff, J. L. Zarestky, H. A. Mook, G. F. Chen, J. L. Luo, N. L. Wang, and P.C. Dai, Nature (London) **453**, 899 (2008).
[2] F. J. Ma, Z. Y. Lu, and T. Xiang, Phys. Rev. B **78**, 224517 (2008).
[3] Y. Kamihara, T. Watanabe, M. Hirano, and H. Hosono, J Am. Chem. Soc. **130**, 3296 (2008).
[4] L. M. Volkova, S. A. Polyshchuk, and F. E. Herbeck, J. Supercond. **13**, 583 (2000).
[5] M. S. D. A. Hussein, M. Daghofer, E. Dagotto, and A. Moreo, Phys. Rev. B **98**, 035124 (2018).
[6] X. J. Zhou, G. D. Liu, J. Q. Meng, W. T. Zhang, H. Y. Liu, L. Zhao, and X. W. Jia, Phys. Status. Solidi. A **207**, 2674 (2010).
[7] K. K. Li, D. D. Yuan, J. G. Guo, and X. L. Chen, Phys. Rev. B **97**, 134503 (2018).
[8] M. Imada, A. Fujimori, and Y. Tokuo, Rev. Mod. Phys. **70**, 1039 (2018).
[9] F. Izumi, J. Solid. State. Chem. **38**, 381 (1981).
[10] H. Giefers, S. Koval, G. Wortmann, W. Sturhahn, E. E. Alp, and M. Y. Hu, Phys. Rev. B **74**, 094303 (2006).
[11] X. Wang, F. X. Zhang, I. Loa, K. Syassen, M. Hanfland, and Y. L. Mathis, phys. status solidi (b) **241**, 3168 (2004).
[12] Y. Q. Guo, R. Q. Tan, X. Li, J. H. Zhao, Z. L. Luo, C. Gao, and W. J. Song, Cryst. Eng. Comm. **13**, 5677 (2011).
[13] M. K. Forthaus, K. Sengupta, O. Heyer, N. E. Christensen, A. Svane, K. Syassen, D. I. Khomskii, T. Lorenz, and M. M. Abd-Elmeguid, Phys. Rev. Lett. **105**, 157001 (2010).
[14] F. C. Hsu *et al.*, P. Natl. Acad. Sci. USA **105**, 14262 (2008).
[15] K. M. Krishna, M. Sharon, M. K. Mishra, and V. R. Marathe, Electrochim Acta **41**, 1999 (1996).
[16] N. E. Christensen, A. Svane, and E. L. Peltzery Blancá, Phys. Rev. B **72**, 014109 (2005).
[17] J. A. McLeod, A. V. Lukoyanov, E. Z. Kurmaev, L. D. Finkelstein, and A. Moewes, JETP Lett. **94**, 142 (2011).
[18] P. -J. Chen and H. -T Jeng, Sci. Rep. **5**, 16359 (2015).
[19] D. M. Adams, A. G. Christy, J. Haines, and S. M. Clark, Phys. Rev. B **46**, 11358 (1992).
[20] H. Giefers, F. Porsch, and G. Wortmann, Phys. B **373**, 76 (2006).
[21] J. Zhang, Y. H. Han, C. L. Liu, W. B. Wu, Y. Li, Q. L. Wang, N. N. Su, Y. Q. Li, B. H. Ma, Y. Z. Ma, and C. X. Cao, J. Phys. Chem. C **115**, 20710 (2011).
[22] W. Guo, L. Fu, Y. Zhang, K. Zhang, L. Y. Liang, Z. M. Liu, H. T. Cao, and X. Q. Pan, Appl. Phys. Lett. **96**, 042113 (2010).
[23] Y. Ogo, H. Hiramatsu, K. Nomura, H. Yanagi, T. Kamiya, M. Hirano, and H. Hosono, Appl. Phys. Lett. **93**, 032113 (2008).
[24] A. Boultif and D. Louer, J. Appl. Cryst. **37**, 724 (2004).
[25] N. Mori, H. Takahashi, and N. Takeshita, High Pressure Res. **24**, 225 (2004).
[26] See Supplemental Material at http://link.aps.org/supplemental/10.1103/PhysRevB.101.104501 for single-crystal XRD analysis results of SnO.
[27] W. K. Choi, H. Sung, K. H. Kim, J. S. Cho, S. C. Choi, H.-J. Jung, S. K. Koh, C. M. Lee, and K. Jeong, J. Mater. Sci. Lett. **16**, 1551 (1997).
[28] K. Gofryk, D. Kaczorowski, T. Plackowski, A. Leithe-Jasper, and Y. Grin, Phys. Rev. B **72**, 094409 (2005).
[29] A. I. Chumakov, G. Monaco, A. Monaco, W. A. Crichton, A. Bosak, R. Ruffer, A. Meyer, F. Kargl, L. Comez, D. Fioretto *et al.*, Phys. Rev. Lett. **106**, 225501 (2011).
[30] J. Guo, J.-i. Yamaura, H. Lei, S. Matsuishi, Y. Qi, and H. Hosono, Phys. Rev. B **88**, 140507 (2013).
[31] W. L. McMillan, Phys. Rev. B. **167**, 331 (1968).
[32] J. Bardeen, L. N. Cooper, and J. R. Schrieffer, Phys. Rev. **108**, 1175 (1957).
[33] A. I. Golovashkin, A. V. Gudenko, A. M. Tskhovrebov, L. N. Zherikhina, and M. L. Norton, Phys. C **235**, 1481 (1994).